Highly Effective Dual Transition Metal Macrocycle Based Electrocatalyst with Macro-/Mesoporous Structures for Oxygen Reduction Reaction

Xinxin Jin, Yan Xie * and Jiahui Huang *

Gold Catalysis Research Center, State Key Laboratory of Catalysis, Dalian Institute of Chemical Physics, Chinese Academy of Sciences, 457 Zhongshan Road, Dalian 116023, China; jinxinxin@dicp.ac.cn

* Correspondence: yanxie@dicp.ac.cn (Y.X.); jiahuihuang@dicp.ac.cn (J.H.); Tel.: +86-411-8246-3017 (Y.X.); +86-411-8246-3012 (J.H.)

Abstract: Metal macrocycle based non-noble metal electrocatalysts (NNMEs) with highly efficient oxygen reduction reaction (ORR) activity, good stability, and excellent resistance to the methanol cross-over effect have been regarded as one of the most important alternatives for Pt or Pt based alloys, which are widely used in fuel cells. However, the expensive price of most metal macrocycles hinder further investigation of such a family of NNMEs in large production for practical applications. Here, we introduce a simple strategy to synthesize metal macrocycle based porous carbon (MMPC) material with low cost and easy production of metal macrocycles (hemin (Hm) and vitamin B_{12} (VB_{12})) as raw materials by using a hard template of MgO. The pyrolysis of MMPC under the optimal temperature at 900 °C shows comparative ORR performance relative to commercial Pt/C, which could be attributed to the large surface area, macro-/mesoporous structure, the carbon layer encapsulating transition metal based oxides, as well as N-doped carbon species. In addition, MMPC (900) displays a better electrochemical property than 20 wt % Pt/C in terms of durability and tolerance to methanol in O_2-saturated 0.1 M KOH media.

Keywords: metal macrocycle; macro-/mesoporous structure; oxygen reduction reaction; fuel cell

1. Introduction

The oxygen reduction reaction (ORR) is a significant process in the cathodes of fuel cells, which is highly desirable to satisfy the urgent demand of electric vehicles. Up to now, the ORR electrocatalysts are still limited on Pt or its alloys in fuel cells. Based on the projected cost for large scale fuel cell production from the United States Department of Energy (DOE) in 2007, Pt-based electrocatalyst layers comprise 56% of the cost in a fuel cell stack [1,2]. At this juncture, the high price and scarcity of Pt is the crucial factor that limits the application of fuel cells in electric vehicles. Therefore, durable and earth-abundant alternatives with high performance, especially non-noble metal electrocatalysts (NNMEs), have been screened by virtue of advanced science and technology. Recently, NNMEs have been divided into several species, namely metal macrocycles (Me-N_4) [3,4], metal oxides [5,6], metal-nitrogen/carbon (Me-N/C), metal carbide [7,8], metal sulfide [9], and metal-free doped carbon matrix [10–12]. Among them, metal macrocycle (like porphyrin and phthalocyanine) based NNMEs are considered to be one of the most promising alternatives both in alkaline media and acidic solution.

In 1964, Jasinski found that cobalt phthalocyanine (CoPc) showed electrocatalytic activity towards ORR [13]. Since then, extensive exploration has been conducted on the study of metal macrocyclic compounds (porphyrin, phthalocyanine, and tetraazannulene) for ORR in both alkaline and acidic media. Later work was performed to improve their stability by supporting FeN_4 or CoN_4 macrocycles

on carbon materials [14]. In addition, electrocatalysts with large surface area were fabricated via various approaches by using carbon materials as supports or constructing porous architectures by using templates to enhance ORR performance [15–18]. Very recently, Song and coworkers reported unprecedented core/shell structured NNMEs through a simple carbonization of evaporation-induced self-assembled 5,10,15,20-tetrakis (4-methoxyphenyl)-21H,23H-porphine iron(III) chloride (FeTMPPCl) layers uniformly coated on carbon black. Such NNMEs exhibited outstanding ORR performance in both alkaline (half-wave potential-$E_{1/2}$ of 0.87 V vs. reversible hydrogen electrode-RHE) and acidic ($E_{1/2}$ = 0.75 vs. RHE) solutions [17]. Joo and coworkers reported a new family of NNMEs based on ordered mesoporous porphyrinic carbons (OMPC) with high surface area and tunable pore structures by nanocasting mesoporous silica templates with FeTMPPCl and CoTMPP as precursors [18]. The obtained FeCo-OMPC showed high electrocatalytic activity ($E_{1/2}$ = 0.845 V vs. RHE) in an alkaline medium. Notably, the high-price of most metal macrocyclic compounds hindered broad applications of NNMEs. Therefore, inexpensive metal macrocyclic compounds, like vitamin B_{12} (VB_{12}) and hemin (Hm), which could be easily obtained by mass production, are widely used in the synthesis of NNMEs with porous architectures [19]. Müllen and coworkers reported a family of mesoporous NNMEs by employing VB_{12} and the polyaniline-Fe (PANI-Fe) as precursors with various hard-templates, including silica nanoparticles (NPs), ordered mesoporous silica SBA-15, and montmorillonite (MMT) [16]. In that paper, mesoporous electrocatalyst prepared by using VB_{12} as a precursor and silica NPs as the template displayed remarkable ORR activity ($E_{1/2}$ of 0.79 V, only ~58 mV deviation from Pt/C), high selectivity, and excellent electrochemical stability in acidic solution. However, a hazardous HF solution has to be used to remove the hard template silica, which is not environmentally friendly.

2. Results

In this work we demonstrate a general and efficient strategy to fabricate dual metal-macrocycle based NNMEs using the hard template synthesis and evaporation induced method. Herein, MgO is selected as the hard template because it can be easily removed by aqueous HCl solution. This strategy will allow the embedment of metal-macrocycles (MeN_4, Me = Fe and Co) within a porous carbon skeleton. The synergistic interaction between Fe and Co species originated from Hm and VB_{12} can enhance the ORR activity. As a consequence, metal-macrocycle based porous carbon (MMPC) materials were prepared, which possessed a high surface area of 429 $m^2 \cdot g^{-1}$ and macro-/mesoporous structures with an average mesopore size of 5.25 nm. The MMPC electrocatalyst shows comparable ORR activity to the commercial Pt/C in O_2-saturated 0.1 M KOH solution, and displays very low HO_2^-% (<1.5%) at 0.4 V (vs. RHE) mainly by a four-electron ORR mechanism to catalyze O_2 directly to H_2O. These values are comparable to the commercial Pt/C. Moreover, the MMPC electrocatalyst shows better durability during a 5000 cycle test and better tolerance to methanol than 20 wt % Pt/C in 0.1 M KOH media.

3. Discussion

The typical synthesis route of MMPC is illustrated in Scheme 1. Hm and VB_{12} (the molecular structures of Hm and VB_{12} are shown in Scheme 2) were induced on the surface of MgO by the rotation evaporation method. Then obtained composites were further heat-treated at high temperature (from 600 °C to 900 °C) under a flowing Ar atmosphere, and metal based NPs were formed due to the pyrolysis of Hm or VB_{12}. Aqueous HCl solution (2 M) was used to remove the hard-template MgO and the exposed metal based NPs. Accordingly, a large amount of macropores and mesopores were created among the carbon materials. The final product was noted as MMPC (*T*). (For more details, see the experimental section).
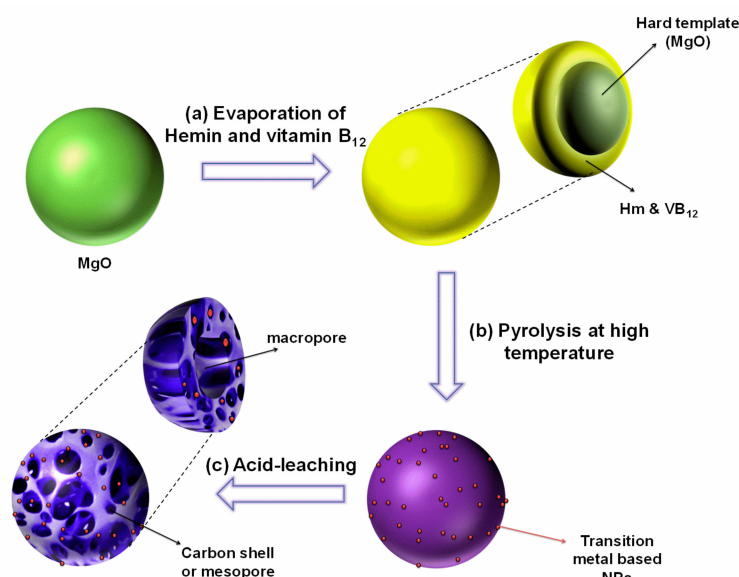
Scheme 1. Illustration of the synthesis route of the metal macrocycle based porous carbon (MMPC) electrocatalyst: (**a**) evaporation of Hemin (Hm) and vitamin B_{12} (VB_{12}) on the surface of MgO; (**b**) heat-treatment step of MMPC; (**c**) acid-leaching process to remove the hard-template and unstable species.
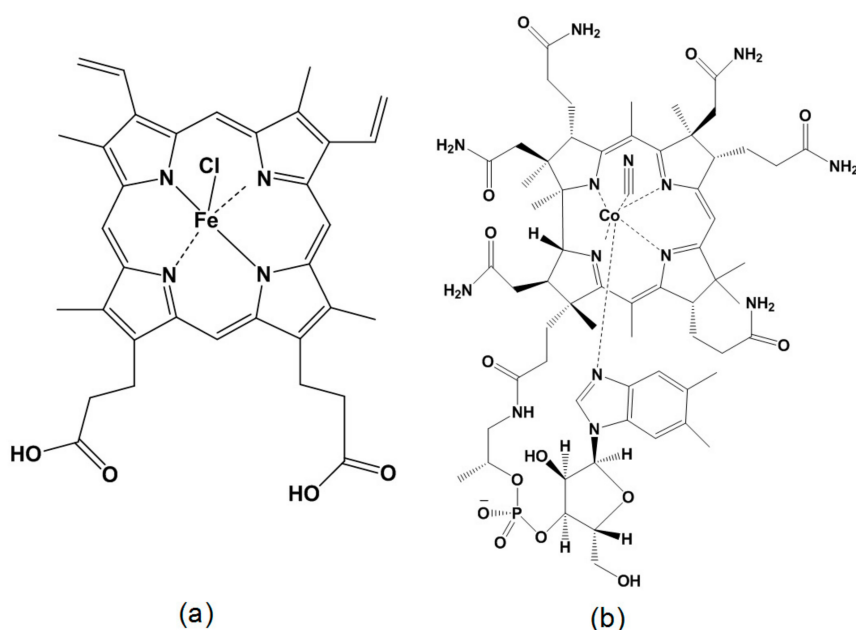

Scheme 2. The molecular structure of Hm (**a**) and VB_{12} (**b**).

The morphology and microstructure of the porous MMPCs were firstly characterized by transmission electron microscopy (TEM, JEOL, Tokyo, Japan). As shown in Figure 1a, the TEM image shows the MMPC with disordered three dimensional macropores, reflecting the removal of the hard-template. Obviously, the metal based NPs encased by graphitic layers in Figure 1b,c, were retained even after the acid-leaching treatment. As shown in the TEM image in Figure 1a, some metal NPs leached out, leaving residual carbon shells decorating the wall of the macropores. The TEM image in Figure 1d reveals that the lattice distance is around 2.1 Å, which is well consistent with the plane (400) of $CoFe_2O_4$ [20,21].
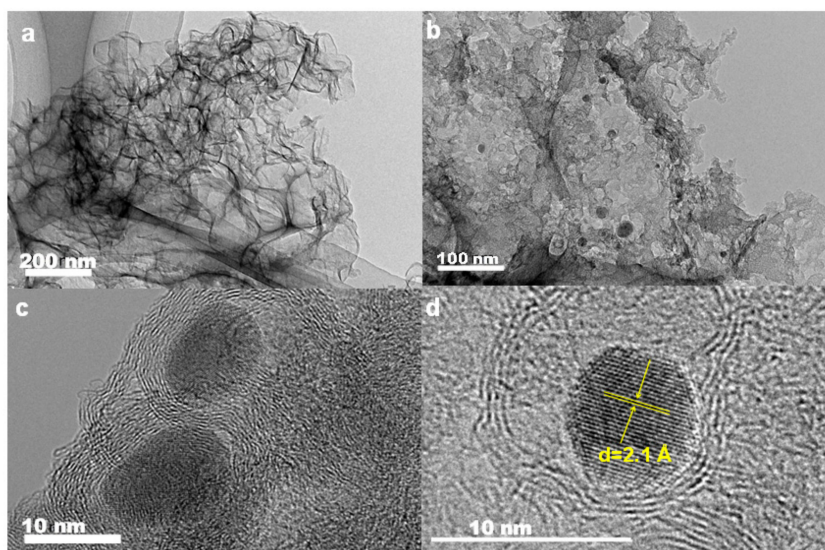
Figure 1. TEM images (**a**–**d**) of the carbonized MMPC followed by acid-leaching.

To gain more information about the MMPC, high angle annular dark field scanning transmission electron microscopy (HAADF-STEM, JEOL, Tokyo, Japan) analysis was carried out. Figure 2a confirms the formation of a large amount of metal based NPs during the pyrolysis of Hm and VB$_{12}$ in Ar atmosphere. Figure 2c shows that nitrogen is uniformly dispersed within the carbon species, which proves the presence of N-doped carbon species. The element mapping of oxygen, cobalt, and iron in Figure 2d–f indicates the existence of metal based oxides.
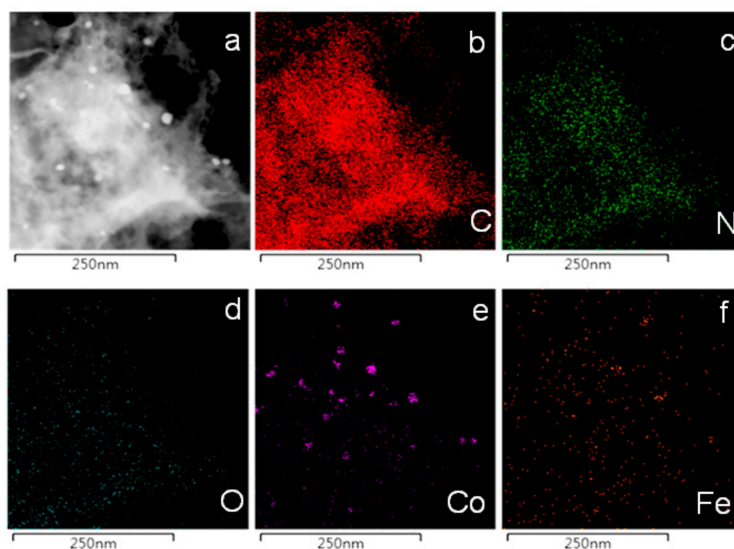
Figure 2. (**a**) The HAADF-STEM image of MMPC (900); the element mapping of (**b**) C; (**c**) N; (**d**) O; (**e**) Co and (**f**) Fe.

To better understand the porous features of the MMPC material, the Barrett-Emmett-Teller (BET) specific surface area and pore size of MMPC were investigated by N$_2$ adsorption-desorption measurements. As shown in Figure 3a,b, MMPC (900) exhibited a typical IV isotherm characteristic for a mesoporous structure. The BET surface area of MMPC (900) was detected to be 429 m$^2 \cdot$g^{-1}, while the electrocatalyst without the MgO hard-template showed a lower BET of only 132 m$^2 \cdot$g^{-1}. This indicates that the macropore creation and high surface area of MMPC (900) is caused by the MgO hard-template.

The effect of pyrolysis temperature on the properties of the MMPC was also investigated. It is noted that the surface area is highly dependent on the pyrolysis temperature (Table 1). The S_{BET} of the MMPC electrocatalyst increases with the pyrolysis temperature from 600 °C to 800 °C, and then decreases with the pyrolysis temperature from 800 °C to 900 °C. This is due to the partial shrinkage of the carbon skeleton at 900 °C. The decrease of S_{mic}, pore volume, and the average mesopore sizes of MMPC (900) in comparison to MMPC (*T*) also favored this analysis Figure 3b shows the formation of large mesopores and macropores in the MMPC electrocatalyst, which will contribute greatly to the pore volume of the MMPC electrocatalyst [22].
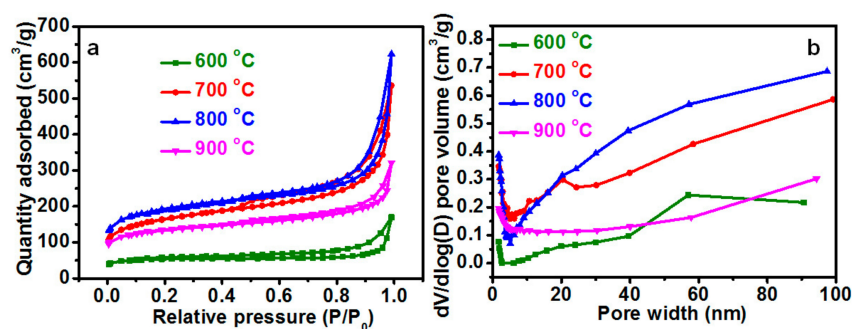

**Figure 3.** (**a**) N_2 adsorption/desorption isotherms and (**b**) the pore size distribution of MMPC (*T*).

Table 1. The physical properties of MMPC (*T*).

MMPC (*T*)	S_{BET} (m²·g⁻¹)	S_{mic} (m²·g⁻¹)	V_t (cm³·g⁻¹)	D_{ave} (nm)
MMPC (600)	168	102	0.26	6.97
MMPC (700)	541	163	0.83	6.51
MMPC (800)	627	236	0.96	6.63
MMPC (900)	429	179	0.50	5.25

　　The sample of MMPC (T) was further characterized by X-ray diffraction (XRD, PANalytical B.V., Almelo, The Netherlands). The typical diffraction peaks of $CoFe_2O_4$ (JCPDS No. 22-1086) were observed in Figure 4a. The broad peaks at about 26° and 44° are indexed to the (002) and (101) planes of graphitic carbon [23,24]. Apparently, these two peaks of MMPC treated under increasing pyrolysis temperatures become stronger and narrower, suggesting the formation of an increasingly ordered graphitic structure. Other peaks located at 30.1°, 35.5°, 43.2°, 53.7°, 57.2° and 62.8° can be ascribed to the diffractions from the crystalline planes (220), (311), (400), (422), (511), and (440) of $CoFe_2O_4$, which agree well with the TEM results in Figure 1d.

　　X-ray photoelectron spectroscopy (XPS, Thermo Scientific, Waltham, MA, USA) was used to analyze the surface elements, indicating the presence of C, N, and O (Figure 4b). It is noted that no obvious peaks of Fe and Co can be detected by XPS (the analysis depth <10 nm). This indicates that Co- and Fe-based NPs were covered by graphitic carbon layers and thus survived during the acid-leaching treatment by the aqueous HCl solution. As shown in Figure 4c, the high-resolution C 1s spectrum of MMPC could be divided into four peaks at 285.0 eV, 286.0 eV, 286.7 eV, and 289.4 eV, assigned to C=C, C=N and C-O, C-N and C=O, and O-C=O, respectively [22]. Such results further confirm the presence of N-doping carbon, O-, and N-containing functional groups in the MMPC electrocatalyst. The content of N is calculated to be about 3.3% relative to the carbon. The high-resolution N 1s spectra can be deconvoluted into four different peaks residing at the binding energy of 398.9 eV, 400.2 eV, 401.3 eV, and 402.8 eV, corresponding to pyridinic N (27.3%), pyrrolic N (19%), graphitic N (40.6%), and oxidized N (13.1%), indicating that nitrogen was indeed doped into the carbon skeletons (Figure 4d). In general, pyridinic N and graphitic N are regarded as sp² hybridized and are able to enhance the ORR performance. Furthermore, the fitted pyridinic N and pyrrolic N atoms can associate with Fe or

Co that originated from Hm and VB$_{12}$ to generate the proposed active sites of Me-N$_x$-C (Me = Fe and Co) [25,26]. Among these N functionalities, the higher content of graphitic N likely plays a dominant role in the determination of the ORR performance [27]. The Fe 2p spectra in Figure 4e shows that the binding energies at around 711.5 eV and 725.0 eV could be due to the 2p$_{3/2}$ and 2p$_{1/2}$ bonds of Fe^{3+} inside the Co$^{(II)}$Fe$^{(III)}_2$O$_4$ oxides. The Co$_{2p}$ spectrum in Figure 4f shows two main peaks at around 780.7 eV and 796.0 eV, as well as two satellites peaks (785.6 eV and 805.5 eV). The peaks at 780.7 eV and 785.6 eV could be assigned to the Co-N species, while the peaks at 796.0 eV and 805.5 eV could originate from Co^{2+} inside of the Co$^{(II)}$Fe$^{(III)}_2$O$_4$ oxides [28–30].
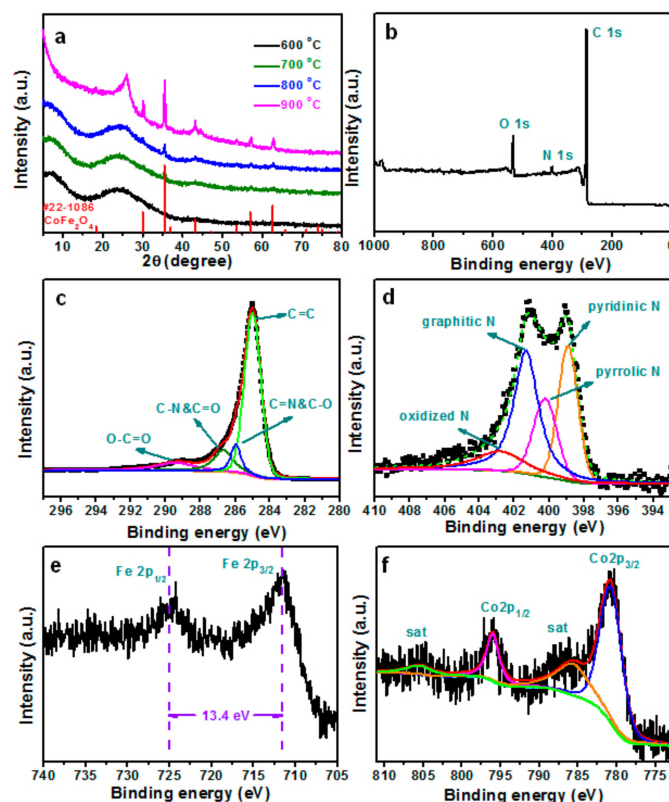
Figure 4. (**a**) X-ray diffraction (XRD) pattern of MMPC (T); (**b**) X-ray photoelectron spectroscopy (XPS) spectra of MMPC (900); high-resolution (**c**) C 1s; (**d**) N 1; (**e**) Fe 2p and (**f**) Co 2p spectra.

As shown in Figure 5a, the diffusion-limited current density of MMPC (900) was 6.15 mA·cm^{-2} at 0.1 V (vs. RHE), much higher than that of MMPC (600), MMPC (700), and MMPC (800), indicating that a higher temperature for carbonization treatment is beneficial for improving the conductivity of the MMPC electrocatalysts. It should be noted that a higher temperature such as 1000 °C was also used to carbonize the MMPC. However, in that case it was very difficult to collect the resulting MMPC materials, probably due to the remarkable shrinkage of the carbon skeleton. On the other hand, different catalyst loading on glassy carbon (GC) was used to try and screen the optimal electrochemical analysis conditions. As shown in Figure 5b and Table 2, the diffusion-limited current density was boosted from 0.2 mg·cm^{-2} to 0.8 mg·cm^{-2}, and the ORR performance is very close to commercial Pt/C in terms of the onset potential (E_{onset}) and $E_{1/2}$ in 0.1 M KOH media. The higher current density of MMPC (900) at 0.8 mg·cm^{-2} results in a slightly higher $E_{1/2}$. Such higher current density may be caused by the thicker catalyst layers coated on the GC, which is not beneficial for the diffusion of reactants and products. Thus, 0.6 mg·cm^{-2} catalyst loading was selected for further investigation. Zelenay and co-workers pointed out that the synergistic effect of Fe and Co could enhance ORR activity and stability [31]. Herein, MMPC electrocatalysts prepared with different molar ratios of Hm and

VB_{12} were also tested in 0.1 M KOH solution (Figure 5c). The different ratios of transition metals also influenced the carbonation process. The outer carbon layer activated by embedded transition metal based oxides would be more active towards ORR performance. The result shows that the best ORR activity was achieved at the molar ratio of Hm to VB_{12} of 3. Taken together, MMPC with the Hm/VB_{12} molar ratio of 3, pyrolyzed at 900 °C and 0.6 mg·cm^{-2} on a GC electrode was chosen for further electrochemical investigation on a rotation disk electrode (RDE) and ring rotation disk electrode (RRDE) in 0.1 M KOH solution. The E_{onset} and $E_{1/2}$ of MMPC (900) is 0.905 V and 0.831 V (vs. RHE), which is a slight 19 mV and 10 mV negative shift relative to the 20 wt % Pt/C in 0.1 M KOH (Figure 5b and Table 2). Compared with the NNMEs reported in the literature, the MMPC electrocatalyst displays excellent and comparable ORR activities in the 0.1 M KOH solution (Table 3).
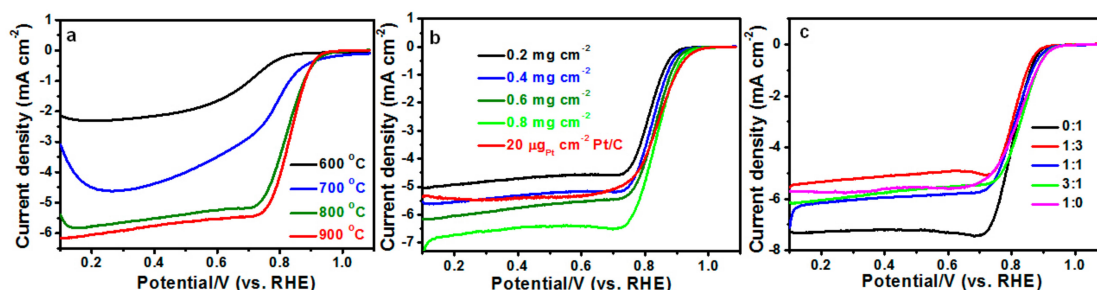
Figure 5. (**a**) Oxygen reduction reaction (ORR) polarization curves of MMPC heat-treated at high temperature from 600 °C to 900 °C in O_2-saturated 0.1 M KOH solution; (**b**) ORR polarization curves of MMPC (900) with the increasing catalyst loading of 0.2 mg·cm^{-2} to 0.8 mg·cm^{-2} on glassy carbon (GC) and commercial Pt/C (20 μg_{Pt}·cm^{-2}); (**c**) ORR polarization curves of MMPCs with various molar ratios of Hm vs. VB_{12} (0:1, 1:3, 1:1, 3:1, and 1:0). Test condition: the rotation rate was 1600 rpm and the scanning rate was 5 mV·s^{-1}.

Table 2. The effect of catalyst loading on E_{onset}, $E_{1/2}$, and current density at 0.8 V of MMPC (900) and commercial Pt/C.

Cat. Loading	E_{onset} (vs. RHE)	$E_{1/2}$ (V vs. RHE)	Current Density at 0.8 V (mA·cm^{-2})
0.2 mg·cm^{-2}	0.878	0.815	2.94
0.4 mg·cm^{-2}	0.894	0.824	3.63
0.6 mg·cm^{-2}	0.905	0.831	4.12
0.8 mg·cm^{-2}	0.919	0.836	4.83
20 μg_{Pt}·cm^{-2}	0.924	0.841	3.97

Table 3. The comparison of ORR performance of the MMPC in this work with the reported non-noble metal electrocatalysts (NNMEs) tested in 0.1 M KOH.

Electrocatalyst	Cat. Loading(mg·cm^{-2})	$E_{1/2}$ (V vs. RHE)	Current Density at 0.8 V (mA·cm^{-2})	Reference
Fe@N–C-700	0.3	0.83	4.15	[32]
CNT/HDC-1000	0.6	0.82	3.25	[33]
NT–G	0.485	0.86	5.00	[34]
Meso/micro-PoPD	0.5	0.87	4.95	[35]
Core/shell NPME	0.6	0.87	5.40	[17]
MMPC (900)	**0.6**	**0.83**	**4.12**	**This work**

To gain more insight into the electrochemical performance of MMPC (900), CV curves were measured in N_2- and O_2-saturated 0.1 M KOH media at a scanning rate of 100 mV·s^{-1}, shown in Figure 6a. Obviously, a characteristic ORR peak was generated in the O_2-saturated electrolyte, which was absent in the CV curve in a N_2-saturated alkaline solution. As shown in Figure 6b, the ORR

polarization curves with increasing rotation speed from 625 rpm to 2025 rpm were recorded in O_2-saturated 0.1 M KOH. The diffusion-limited current density of MMPC (900) becomes larger with the increasing rotation speed. The Koutecky-Levich (K-L) plots collected at different potentials (0.45 V, 0.55 V, 0.65 V, and 0.75 V vs. RHE) in Figure 6c are demonstrated based on the data of Figure 6b, indicating the first-order reaction kinetics toward the concentration of dissolved O_2, from which the electron transfer number (n) can be determined as ~4 based on the K-L equation:

$$\frac{1}{I_D} = \frac{1}{I_K} + \frac{1}{B\omega^{1/2}} \tag{1}$$

where I_D is the measured current density at the disk, I_K is the kinetic current in amperes at a constant potential, ω is the electrode rotation speed in rpm, and B is the reciprocal of the slope that can be determined from the slope of the K-L plot using the Levich equation as below:

$$B = 0.62nFAC_0D_0^{\frac{2}{3}}\nu^{\frac{-1}{6}} \tag{2}$$

in which n is the number of electrons transferred per oxygen molecule, F is the Faraday constant of 96,485 C·mol^{-1}, D_0 of 1.93×10^{-5} cm^2·s^{-1} is the diffusion coefficient of O_2, C_0 of 1.26×10^{-3} mol·cm^{-3} is the bulk concentration of O_2, and ν (0.01009 cm^2·s^{-1}) is the kinematic viscosity of the electrolyte in 0.1 M KOH media.
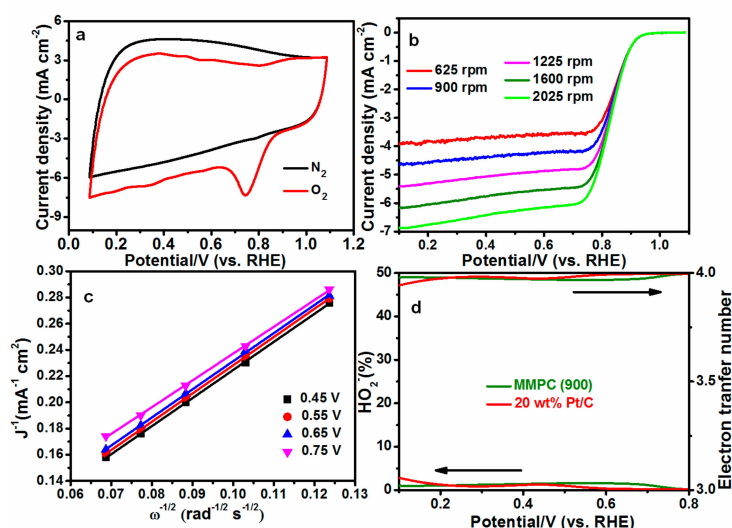
Figure 6. (**a**) Cyclic voltammetry (*CV*) curves of MMPC (900) in N_2 and O_2 at the scanning rate of 100 mV·s^{-1} in 0.1 M KOH solution; (**b**) ORR polarization curves of MMPC (900) with different rotation rates from 625 rpm to 2025 rpm in O_2-saturated 0.1 M KOH; (**c**) Koutecky-Levich plots derived from ORR polarization curves in (**b**) at the selected electrode potentials (0.45, 0.55, 0.65, and 0.75 V vs. reversible hydrogen electrode-RHE); (**d**) HO$_2^-$% yield and n number of MMPCs (900) and commercial Pt/C at the constant potential of 0.2 V vs. Hg/HgO. Note: MMPC (900) synthesized with the molar ratio (3:1) of Hm to VB$_{12}$.

To assess the MMPC (900) electrocatalyst, RRDE measurements of MMPC (900) and commercial Pt/C were conducted in O_2-saturated 0.1 M KOH at 1600 rpm. As shown in Figure 6d, the calculated n number based on Equation (3) from 0.1 V to 0.8 V (vs. RHE) is about 3.98, which is very close to the n number based on the K-L plots, indicating a direct 4e process to catalyze O_2 to H_2O. The HO$_2^-$% yield calculated by Equation (4) is lower than 1.5% at the potential of 0.4 V (vs. RHE) which is slightly higher than that of the commercial Pt/C (<1.2% at 0.4 V).

$$n = 4 \times \frac{I_D}{I_D + I_R/N} \qquad (3)$$

$$\%HO_2^- = 200 \times \frac{I_R/N}{I_D + I_R/N} \qquad (4)$$

where I_D and I_R are the Faradic current at the disk and ring electrode, respectively. The manufacturer's value of N is the H_2O_2 collection coefficient of 37% at the ring electrode.

In practical applications of fuel cells, the long-term durability of the electrocatalyst is another key issue. Here, we conducted the accelerated durability test for MMPC (900) and 20 wt % Pt/C by cycling the catalysts 5000 times between -0.4 V to 0.2 V (vs. Hg/HgO) at a scanning rate of 100 mV·s^{-1}. The changes in $E_{1/2}$ before and after the cycling test indicate that the MMPC (900) electrocatalyst underwent a negative shift of 18 mV with a current density of 3.07 mA·cm^{-2} at 0.8 V (vs. RHE) after 5000 cycles, while Pt/C exhibited an obvious negative shift of 19 mV with a lower current density of 2.79 mA·cm^{-2} at 0.8 V (vs. RHE) after 5000 cycles (Figure 7a). Then, we investigated the tolerance of MMPC (900) and Pt/C against methanol in O_2-saturated 0.1 M KOH solution with an additional injection of 10 *v/v* % methanol (Figure 7b). The result indicates that MMPC (900) exhibits a good selectivity of ORR, while commercial Pt/C shows an obvious decay due to the vulnerability of Pt to methanol attack.
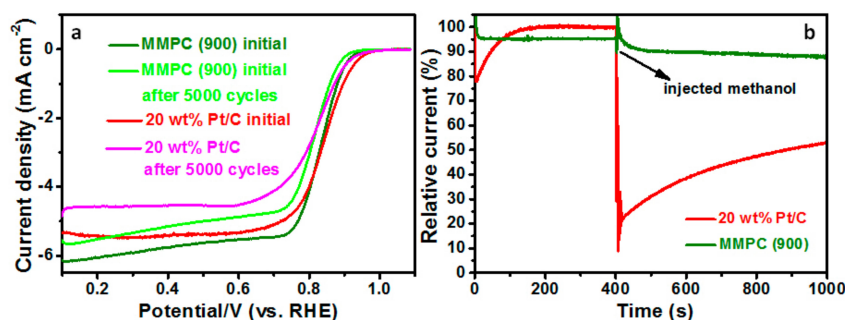
Figure 7. (**a**) ORR polarization curves of MMPC (900) and commercial Pt/C before and after 5000 cycles at the scanning rate of 5 mV·s^{-1} in 0.1 M KOH solution; (**b**) chronoamperometric responses at -0.3 V (vs. Hg/HgO) in O_2-saturated 0.1 M KOH at MMPC (900) and Pt/C at 1600 rpm before and after addition of 10 *v/v* % methanol.

4. Materials and Methods

4.1. Materials

All materials were used directly as received. Magnesium oxide (MgO, 99.9%, $d \approx 50$ nm), Hemin (Hm, 98%), and vitamin B$_{12}$ (VB$_{12}$, 98%) were purchased from Aladdin. Ethanol was purchased from Sinopharm Chemical Reagent Co., Ltd., Shanghai, China. Commercial 20 wt % Pt/C electrocatalyst was purchased from Johnson Matthey (JM) Company, London, UK. Milli-Q water (resistivity 18.2 MΩ·cm at 25 °C) was used in all experiments.

4.2. Synthesis of Metal-Macrocycle Based Porous Carbon (MMPC)

In a typical procedure, 70 mg of commercial MgO nanospheres ($d \approx 50$ nm) was dispersed in 50 mL ethanol under sonication, and 17.7 mg Hm and 12.3 mg VB$_{12}$ (i.e., the molar feed ratio of Hm and VB$_{12}$ was 3:1) were added into the solution. The obtained mixture was sonicated for 30 min before using evaporation technology to remove the ethanol, and the collected solid composites were dried overnight at room temperature in the vacuum oven. The solid composites were then thermally treated under an Ar atmosphere at high temperature from 600 °C to 900 °C for 2 h. The final product was treated by acid leaching with 2 M HCl solution overnight to remove the hard template and was then washed with deionized water until the filtrate became neutral. For comparison, different molar ratios

of Hm and VB_{12} (1:0, 1:1, 1:3, 3:1, and 0:1) and the NNME synthesized without using the hard-template were used to synthesize MMPC for catalyzing the ORR.

4.3. Characterization

X-ray powder diffraction (XRD) was recorded on a PANalytical Empyrean-100 diffractometer with Cu Kα radiation at a scanning rate at $6°·min^{-1}$. Porous structures were determined by nitrogen adsorption/desorption at 77 K using an automatic adsorption system (ASAP2020, Micromeritics, Norcross, GA, USA). Samples were degassed at 250 °C for 5 h prior to the measurement. The specific surface area (S_{BET}) of the samples was calculated using the Brunauer-Emmett-Teller (BET) method, the micropore area (S_{mic}) was calculated using the *t*-plot method, the total pore volume (V_t) was estimated from single point adsorption at a relative pressure P/P_0 of 0.99, and the pore size distributions (D_{ave}) of all samples were derived from the density functional theory (DFT) model. X-ray photoelectron spectroscopy (XPS) was carried out on a Thermo ESCALAB 250Xi photoelectron spectrometer. Transmission electron microscopy (TEM), high resolution TEM (HRTEM), and element mapping were operated on a JEM-2100F at 200 kV.

4.4. Electrocatalytic Activity Measurements

The electrochemical measurements were carried out in a conventional three-electrode cell by CHI 760E (CH Instruments, Shanghai, China) and a VSP-300 electrochemical workstation (BioLogic, Claix, France) at 25 °C. The catalyst-coated glassy carbon (GC) disk, Hg/HgO, and Pt net were used as a working electrode, a reference electrode, and a counter electrode, respectively. All the potentials in this work refer to that of the reversible hydrogen electrode (RHE) as $E_{(RHE)} = E_{(Hg/HgO)} + 0.887$ V (Figure 8). The electrocatalyst ink was prepared to be 2 mg·mL^{-1} with ethanol, ultrapure water, and 5 wt % Nafion ($V_{ethanol}:V_{water}:V_{Nafion}$ = 9:1:0.1). After sonicating for at least 5 min, 60 μL of ink was coated on the surface of the GC electrode of the RDE (the geometric surface area of the GC was 0.19625 cm^2) to obtain the catalyst loading of ~0.6 mg·cm^{-2}. The JM 20 wt % Pt/C with Pt loading of 20 μg·cm^{-2} was prepared by coating 20 μL of 1 mg·mL^{-1} Pt/C ink on the GC. Cyclic voltammetry (*CV*) curves were evaluated to clean the surface of electrocatalysts by purging with N_2 for at least 10 min in 0.1 M KOH solution. The potential range was from 0.1 V to 1.1 V (vs. RHE) and the scanning rate was 100 mV·s^{-1}. Then *CV* curves in O_2-saturated alkaline solution were conducted under the same condition. The RDE test was recorded to measure the ORR polarization curves with different rotation rates from 625 rpm to 2025 rpm during the range from 0.1 to 1.1 V (vs. RHE) in 0.1 M KOH solution. The rotating ring disk electrode (RRDE) with a disk surface area of 0.2475 cm^2 was used to obtain the ORR polarization curves in O_2-saturated 0.1 M KOH media from 0.1 V to 1.1 V (vs. RHE) with a scanning rate of 5 mV·s^{-1} at 1600 rpm under a constant potential of 0.2 V (vs. Hg/HgO).
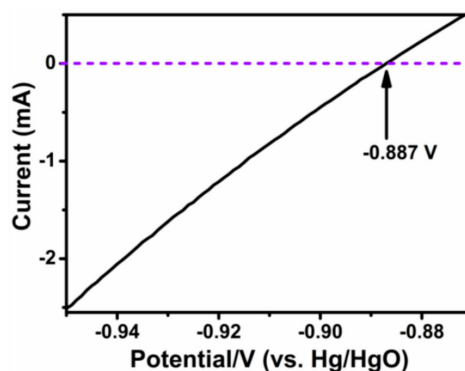
Figure 8. LSV curve recorded at 25 °C in H_2-saturated 0.1 M KOH media with a scanning rate of 1 mV·s^{-1}. Here, Pt net was used as working electrode. The thermodynamic equilibrium potential for H^+/H_2 reaction [18] was determined as zero current.

5. Conclusions

In summary, we have successfully prepared MMPC electrocatalysts as a novel NNME through a facile synthetic approach by using MgO as a hard-template, Hm and VB_{12} as transition metal based N-doped carbon sources, respectively. Various characterizations revealed that the $CoFe_2O_4$ NPs were well encapsulated within the N-doped porous carbon materials. Among the MMPC electrocatalysts, MMPC (900) shows a comparative ORR activity relative to commercial Pt/C, which should be mainly ascribed to the high surface area, the mixed macro-/mesoporous structure, the outer carbon layers encapsulating $CoFe_2O_4$, and the N-doped carbon species. Compared with commercial Pt/C, MMPC (900) even shows better durability and tolerance to methanol.

Author Contributions: Yan Xie conceived and designed the experiments; Xinxin Jin performed the experiments; Xinxin Jin and Yan Xie analyzed the data; Yan Xie and Jiahui Huang wrote the paper.

Conflicts of Interest: The authors declare no conflict of interest.

References

1. James, B.; Kalinoski, J. Mass-production cost estimation of automotive fuel cell system. In Proceedings of the DOE-EERE Fuel Cell Technologies Program-2009 DOE Hydrogen Program Review, Arlington, VA, USA, 21 May 2009.
2. Sinha, J.; Lasher, S.; Yang, Y. Direct Hydrogen PEMFC Manufacturing Cost Estimation for Automotive Application. In Proceedings of the DOE-EERE Fuel Cell Technologies Program-2009 DOE Hydrogen Program Review, Arlington, VA, USA, 21 May 2009.
3. Liu, H.S.; Song, C.J.; Tang, Y.H.; Zhang, J.L.; Zhang, J.J. High-surface-area CoTMPP/C synthesized by ultrasonic spray pyrolysis for PEM fuel cell electrocatalysts. *Electrochim. Acta* **2007**, *52*, 4532–4538. [CrossRef]
4. Wu, Z.S.; Chen, L.; Liu, J.Z.; Parvez, K.; Liang, H.W.; Shu, J.; Sachdev, H.; Graf, R.; Feng, X.L.; Müllen, K. High-performance electrocatalysts for oxygen reduction derived from cobalt porphyrin-based conjugated mesoporous polymers. *Adv. Mater.* **2014**, *26*, 1450–1455. [CrossRef] [PubMed]
5. Liang, Y.Y.; Li, Y.G.; Wang, H.L.; Zhou, J.G.; Wang, J.; Regier, T.; Dai, H.J. Co_3O_4 nanocrystals on graphene as a synergistic catalyst for oxygen reduction reaction. *Nat. Mater.* **2011**, *10*, 780–786. [CrossRef] [PubMed]
6. Liang, Y.Y.; Wang, H.L.; Zhou, J.G.; Li, Y.G.; Wang, J.; Regier, T.; Dai, H.J. Covalent hybrid of spinel manganese-cobalt oxide and graphene as advanced oxygen reduction electrocatalysts. *J. Am. Chem. Soc.* **2012**, *134*, 3517–3523. [CrossRef] [PubMed]
7. Hu, Y.; Jensen, J.O.; Zhang, W.; Cleemann, L.N.; Xing, W.; Bjerrum, N.J.; Li, Q.F. Hollow spheres of iron carbide nanoparticles encased in graphitic layers as oxygen reduction catalysts. *Angew. Chem. Int. Ed.* **2014**, *53*, 3675–3679. [CrossRef] [PubMed]
8. Xiao, M.L.; Zhu, J.B.; Feng, L.G.; Liu, C.P.; Xing, W. Meso/macroporous nitrogen-doped carbon architectures with iron carbide encapsulated in graphitic layers as an efficient and robust catalyst for the oxygen reduction reaction in both acidic and alkaline solutions. *Adv. Mater.* **2015**, *27*, 2521–2527. [CrossRef] [PubMed]
9. Zhu, Y.S.; Zhang, B.S.; Liu, X.; Wang, D.W.; Su, D.S. Unravelling the structure of electrocatalytically active Fe-N complexes in carbon for the oxygen reduction reaction. *Angew. Chem. Int. Ed.* **2014**, *53*, 10673–10677. [CrossRef] [PubMed]
10. Yang, L.J.; Jiang, S.J.; Zhao, Y.; Zhu, L.; Chen, S.; Wang, X.Z.; Wu, Q.; Ma, J.; Ma, Y.W.; Hu, Z. Boron-doped carbon nanotubes as metal-free electrocatalysts for the oxygen reduction reaction. *Angew. Chem. Int. Ed.* **2011**, *50*, 7132–7135. [CrossRef] [PubMed]
11. Yang, D.S.; Bhattacharjya, D.; Inamdar, S.; Park, J.; Yu, J.S. Phosphorus-doped ordered mesoporous carbons with different lengths as efficient metal-free electrocatalysts for oxygen reduction reaction in alkaline media. *J. Am. Chem. Soc.* **2012**, *134*, 16127–16130. [CrossRef] [PubMed]
12. Gong, K.P.; Du, F.; Xia, Z.H.; Durstock, M.; Dai, L.M. Nitrogen-doped carbon nanotube arrays with high electrocatalytic activity for oxygen reduction. *Science* **2009**, *323*, 760–764. [CrossRef] [PubMed]
13. Jasinski, R. A new fuel cell cathode catalyst. *Nature* **1964**, *201*, 1212–1213. [CrossRef]

14. Scherson, D.A.; Gupta, S.L.; Fierro, C.; Yeager, E.B.; Kordesch, M.E.; Eldridge, J.; Hoffman, R.W.; Blue, J. Cobalt tetramethoxyphenyl porphyrin-emission Mossbauer spectroscopy and O_2 reduction electrochemical studies. *Electrochim. Acta* **1983**, *28*, 1205–1209. [CrossRef]

15. Jiang, Y.; Xie, Y.; Jin, X.X.; Hu, Q.; Chen, L.; Xu, L.; Huang, J.H. Highly efficient iron phthalocyanine based porous carbon electrocatalysts for the oxygen reduction reaction. *RSC Adv.* **2016**, *6*, 78737–78742. [CrossRef]

16. Liang, H.W.; Wei, W.; Wu, Z.S.; Feng, X.L.; Müllen, K. Mesoporous metal-nitrogen-doped carbon electrocatalysts for highly efficient oxygen reduction reaction. *J. Am. Chem. Soc.* **2013**, *135*, 16002–16005. [CrossRef] [PubMed]

17. Li, J.; Song, Y.J.; Zhang, G.X.; Liu, H.Y.; Wang, Y.R.; Sun, S.H.; Guo, X.W. Pyrolysis of selfassembled iron porphyrin on carbon black as core/shell structured electrocatalysts for highly efficient oxygen reduction in both alkaline and acidic medium. *Adv. Funct. Mater.* **2017**, *27*, 1604356. [CrossRef]

18. Cheon, J.Y.; Kim, T.; Choi, Y.M.; Jeong, H.Y.; Kim, M.G.; Sa, Y.J.; Kim, J.; Lee, Z.; Yang, T.H.; Kwon, K.; et al. Ordered mesoporous porphyrinic carbons with very high electrocatalytic activity for the oxygen reduction reaction. *Sci. Rep.* **2013**, *3*. [CrossRef] [PubMed]

19. Xie, Y.; Tang, C.Z.; Hao, Z.Q.; Lv, Y.; Yang, R.X.; Wei, X.M.; Deng, W.Q.; Wang, A.J.; Yi, B.L.; Song, Y.J. Carbonization of self-assembled nanoporous hemin with a significantly enhanced activity for the oxygen reduction reaction. *Faraday Discuss.* **2014**, *176*, 393–408. [CrossRef] [PubMed]

20. Xia, H.; Zhu, D.; Fu, Y.; Wang, X. $CoFe_2O_4$-graphene nanocomposite as a high-capacity anode material for lithium-ion batteries. *Electrochim. Acta* **2012**, *83*, 166–174. [CrossRef]

21. Liu, J.X.; Liang, J.; Zhou, H.; Xiao, C.H.; Liang, F.X.; Ding, S.J. $CoFe_2O_4$ nanoparticles anchored on bowl-like carbon backbone for enhanced reversible lithium storage. *RSC Adv.* **2016**, *6*, 50153–50157. [CrossRef]

22. Su, Y.H.; Jiang, H.L.; Zhu, Y.H.; Yang, X.L.; Shen, J.H.; Zou, W.J.; Chen, J.D.; Li, C.Z. Enriched graphitic N-doped carbon-supported Fe_3O_4 nanoparticles as efficient electrocatalysts for oxygen reduction reaction. *J. Mater. Chem. A* **2014**, *2*, 7281–7287. [CrossRef]

23. Ferrero, G.A.; Preuss, K.; Marinovic, A.; Jorge, A.B.; Mansor, N.; Brett, D.J.; Fuertes, A.B.; Sevilla, M.; Titirici, M.M. Fe-N-doped carbon capsules with outstanding electrochemical performance and stability for the oxygen reduction reaction in both acid and alkaline conditions. *ACS Nano* **2016**, *10*, 5922–5932. [CrossRef] [PubMed]

24. Yang, J.; Hu, J.; Weng, M.; Tan, R.; Tian, L.; Yang, J.; Amine, J.; Zheng, J.; Chen, H.; Pan, F. Fe-cluster pushing electrons to N-doped graphitic layers with Fe_3C (Fe) hybrid nanostructure to enhance O_2 reduction catalysis of Zn-Air batteries. *ACS Appl. Mater. Interfaces* **2017**, *9*, 4587–4596. [CrossRef] [PubMed]

25. Lin, L.; Zhu, Q.; Xu, A.W. Noble-metal-free Fe-N/C catalyst for highly efficient oxygen reduction reaction under both alkaline and acidic conditions. *J. Am. Chem. Soc.* **2014**, *136*, 11027–11033. [CrossRef] [PubMed]

26. Liu, R.L.; Wu, D.Q.; Feng, X.L.; Müllen, K. Nitrogen-doped ordered mesoporous graphitic arrays with high electrocatalytic activity for oxygen reduction. *Angew. Chem. Int. Ed.* **2010**, *49*, 2565–2569. [CrossRef] [PubMed]

27. Niu, W.H.; Li, L.G.; Liu, X.J.; Wang, N.; Liu, J.; Zhou, W.J.; Tang, Z.H.; Chen, S.W. Mesoporous N-doped carbons prepared with thermally removable nanoparticle templates: An efficient electrocatalyst for oxygen reduction reaction. *J. Am. Chem. Soc.* **2015**, *137*, 5555–5562. [CrossRef] [PubMed]

28. Long, N.V.; Yang, Y.; Teranishi, T.; Thi, C.M.; Cao, Y.Q.; Nogami, M. Related magnetic properties of $CoFe_2O_4$ cobalt ferrite particles synthesised by the polyol method with $NaBH_4$ and heat treatment: new micro and nanoscale structures. *RSC Adv.* **2015**, *5*, 56560–56569. [CrossRef]

29. Wu, G.; Chen, Z.W.; Artyushkova, K.; Garzon, F.H.; Zelenay, P. Polyaniline-derived non-precious catalyst for the polymer electrolyte fuel cell cathode. *ECS Trans.* **2008**, *16*, 159–170.

30. Li, S.; Wu, D.Q.; Liang, H.W.; Wang, J.Z.; Zhuang, X.D.; Mai, Y.Y.; Su, Y.Z.; Feng, X.L. Metal-nitrogen doping of mesoporous carbon/graphene nanosheets by self-templating for oxygen reduction electrocatalysts. *ChemSusChem* **2014**, *7*, 3002–3006. [CrossRef] [PubMed]

31. Wu, G.; More, K.L.; Johnston, C.M.; Zelenay, P. High-performance electrocatalysts for oxygen reduction derived from polyaniline, iron, and cobalt. *Science* **2011**, *332*, 443–447. [CrossRef] [PubMed]

32. Wang, J.; Wu, H.H.; Gao, D.F.; Miao, S.; Wang, G.X.; Bao, X.H. High-density iron nanoparticles encapsulated within nitrogen-doped carbon nanoshell as efficient oxygen electrocatalyst for zinc-air battery. *Nano Energy* **2015**, *13*, 387–396. [CrossRef]

33. Sa, Y.J.; Park, C.Y.; Jeong, H.Y.; Park, S.H.; Lee, Z.H.; Kim, K.T.; Park, G.G.; Joo, S.H. Carbon nanotubes/heteroatom-doped carbon core-sheath nanostructures as highly active, metal-free oxygen reduction electrocatalysts for alkaline fuel cells. *Angew. Chem. Int. Ed.* **2014**, *53*, 4102–4106. [CrossRef] [PubMed]

34. Li, Y.G.; Zhou, W.; Wang, H.L.; Xie, L.M.; Liang, Y.Y.; Wei, F.; Idrobo, J.C.; Pennycook, S.J.; Dai, H.J. An oxygen reduction electrocatalyst based on carbon nanotube-graphene complexes. *Nat. Nanotechnol.* **2012**, *7*, 394–400. [CrossRef] [PubMed]

35. Liang, H.W.; Zhuang, X.D.; Brüller, S.; Feng, X.L.; Müllen, K. Hierarchically porous carbons with optimized nitrogen doping as highly active electrocatalysts for oxygen reduction. *Nat. Commun.* **2014**, *5*, 4973. [CrossRef] [PubMed]